Supporting Information

Unraveling the Local Coordination Effect of Cu-N-C Single-Atom Catalyst towards CO Adsorption via Gas-Phase Cluster Model Approach

Qing Wang[a,b], Dingding Lv[a], Jian Zhou[a,b], Detong Kong[a], Shanshan Lin[a,b], Lili Zhang[a,b], Zhen-an Qiao[c], Yuxiao Ding[b,d]*, and Xiaoyan Sun[a,b]*

[a.] State Key Laboratory of Photoelectric Conversion and Utilization of Solar Energy, Qingdao New Energy Shandong Laboratory, Qingdao Institute of Bioenergy and Bioprocess Technology, Chinese Academy of Sciences, Qingdao 266101, China
[b.] University of Chinese Academy of Sciences, Beijing 100049, China.
[c.] State Key Laboratory of Inorganic Synthesis and Preparative Chemistry, Jilin University, Changchun, 130012, China.
[d.] State Key Laboratory of Low Carbon Catalysis and Carbon Dioxide Utilization Lanzhou Institute of Chemical Physics, Chinese Academy of Sciences, Lanzhou, 730000, China
Corresponding author: yuxiaoding@licp.cas.cn; sunxy@qibebt.ac.cn

Table of Contents

1. Supplementary Text

1.1 Experimental Methods

The mass spectrometric experiments for the reactions of $[CuL]^+$ and $[Cu]^+$ ions were performed on a LTQ XL linear quadrupole ion-trap mass spectrometer (LTQ XL, Thermo Fisher Scientific) equipped with an electrospray ionization (ESI) source operating in positive ion mode. The reasons for choosing an ion trap as the reaction vessel are as follows: ① Ion traps very efficiently lock ions into stable trajectories so relatively long residence times are possible[1]; ② The trapping field in an ion trap is robust so collisions are not problematic and do not lead to significant ion loss. In fact, quadrupole ion traps are generally operated with the addition of a helium buffer gas at a pressure of approximately 1 mtorr[1]. Therefore, reactions in an ion trap can be considered as "multi-collision" reaction with the greater collisional stabilization compared to Fourier-transform ion cyclotron resonance (FT-ICR)[2]; ③ the reactant ions generally are very close to the temperature of the helium buffer gas (~300 K)[1]. The instrument was in-house modified to allow the introduction of reagent gases into the trap and study the reactivity of mass-selected ions with limited amount toward neutral species under continuous flow conditions. The pressure of the neutral gases introduced into the trap was kept constant by a Granville–Phillips leak valve and measured by a Granville–Phillips Series 342 Stabil Ion Vacuum Gauge (accuracy 5% of reading). This modification is feasible as demonstrated in many previous studies[3-6]. In addition, water and solvent molecules cannot thoroughly be eliminated from the apparatus, which may lead to some loss of reactant ions. Therefore, the single most intense peak was mass selected to follow the course of reactions and we calculated the reaction rate branching ratio by determining the ratio of CO to background gas adsorption signals (**Table S1**), thus eliminating background gas interference and obtaining a more accurate reaction rate.

Samples were injected operating at 5 mL min^{-1} via the onboard syringe pump connected to an ESI source. Nitrogen was used as a sheath and auxiliary gas with a capillary temperature at 275 °C and a spray voltage at 4 kV, and thus the parent ions were initially formed in the source. Then the clusters of interest were mass-selected by a linear ion trap (LIT), and the target ions were generated by CID or direct isolation. By spraying a millimolar solution of $Cu(NO_3)_2 \cdot 3H_2O$ and a sequence of ligands dissolved in methanol, $[CuL]^+$ or their precursor ions were generated and detected taking advantage of the MS^n function of the mass spectrometer. Gaseous reactant CO was introduced into the ion trap via a flowmeter and measured by an ion vacuum gauge, and ion–molecule reactions were further performed and monitored when Cu-centered species were isolated.

1.2 Pseudo-first-order Rate Constant Calculation Formula

We monitored and maintained a constant reaction pressure of approximately 1×10^{-5} Torr by observing the changes in the ion gauge readings before and after gas flow. Pseudo first-order rates were estimated by extrapolation of plots of reactant ion intensity vs reaction time. The reaction time was the time delay between isolation of the reactant ion and its mass analysis[7]. By measuring the abundances of reactants at different reaction times, we calculated the reaction rate. The pseudo-first-order rate constant calculation formula is as follows:

$$ln\frac{I_R}{I_T} = -k'_T t_R \quad (1)$$

$$ln\frac{I_R}{I_T} = -k_T\frac{P_{effective}}{kT}t_R \quad (2)$$

$$N = \frac{P_{effective}V}{kT} \quad (3)$$

$$k_T = \frac{k'_T V}{N} \quad (4)$$

I_R — Peak area of the reactant after the reaction
I_T — Sum of the peak areas of the reactant and all products after the reaction
k_T — First-order reaction rate constant
P_{CO} — The gas pressure of CO in the ion trap, 1×10^{-7} Torr here
k — Boltzmann constant, 1.38×10^{-23} J/K
T — Reaction temperature, generally 298K
t_R — Reaction time
V — Ion trap volume, 1.30×10^5 mm^3
N — Number of reacting molecules

However, due to the presence of water and solvent molecules as impurity gases in the LTQ, the observed reaction rate (k_T) is the total reaction rate. According to the characteristics of parallel reactions, where the product concentration is initially zero, we can get k_{CO} through:

$$\frac{k_{CO}}{k_T} = \frac{I_{CO}}{I_T} \quad (5)$$

1.3 Theoretical Methods

Optimization was carried out using density functional theory within the Gaussian16.A03 program package[8], with the PBE0-D3(BJ)[9-11] functional in conjunction with “Ahlrichs” basis sets def2-TZVPP[12-13] for all atoms. Subsequently, the ORCA 4.2.1 program package[14] was utilized for single point energy calculations at the DLPNO-CCSD(T)/cc-pVTZ level[15-17]. Zero-point vibrations and temperature corrections were taken into account at the PBE0-D3(BJ)/def2-TZVPP level. The input files for the ORCA program were prepared with the assistance of the Multiwfn[18] code. Harmonic vibrational frequency analysis was conducted to confirm that all optimized structures reside at minima on their respective potential energy surfaces. Calculations of CO vibrational frequencies were carried out at the B3LYP/def2-TZVP level[13, 19], which is widely used for similar systems[20]. To address the tendency of the harmonic approximation to overestimate vibrational frequencies, we applied an appropriate frequency scaling factor (0.959) to the calculated results to correct for the systematic errors associated with the computational level[21]. In addition, we obtained the optimized C-O bond lengths at the PBE0/def2-TZVPP level and calculated their deviations from that of free CO. The computational results, as well as the charge on Cu centers, are summarized in **Table S6**. Subsequently, we performed Charge Decomposition Analysis (CDA) calculations to evaluate the Cu←CO σ-donation and Cu→CO π-back donation electron counts[22]. Combined with the Energy Dissociation Analysis (EDA) analysis presented in **Table S3**, we analyzed the underlying reasons for the changes in C-O vibrational frequencies (**Table S7**). Furthermore, Multiwfn was applied for the analysis of sobEDA, valence electron density, and EST-NOCV. The visualization of donor-acceptor interactions and orbitals was facilitated through VESTA[23].

1.4 Bonding Nature Details

To show more bonding nature details between the ligands and Cu center, as well as their interactions with CO, we firstly gave the lowest energy structures of Cu species and their corresponding CO-coordinated products for the reason that collisions with the helium buffer gas can cool reactant ions to near room temperature within a few milliseconds[24]. Since the cooling is significantly faster than the time scale of reactions, ion–molecule reactions in our system proceed at near thermal energies even after subjecting the ion to trapping voltages or CID[25-26]. Please note that $[Cu\text{-}Pyr]^+$ and $[Cu\text{-}Cz]^+$ are characterized as doublet states, $[Cu\text{-}TPP]^+$ is a triplet state, and the remaining complexes are singlet states. The geometric structures of $[CuL]^+$ in **Fig. 2b** are in line with the spectral characterization reported previously[28-31]. Cu atom coordinates with N atoms in the ligands, and CO adsorbed on the Cu active site via carbon-end bonding in the complex, consistent with previously reported findings[30-31]. Energy decomposition analysis (EDA)[32] was employed to understand the interactions between Cu atom and the ligands, as well as that between $[CuL]^+$ and CO (**Tables S2-S3**). The results show that electrostatic attraction and orbital interactions both played critical role in Cu complexes and CO bound species. For a deep dive into orbital interactions, we examined the Mayer bond orders, finding that both the Cu-N and Cu-CO bond orders are close to 1, suggesting a covalent bonding nature (**Table S4**). This can be additionally confirmed by the presence of high valence electron densities at the Cu-CO and Cu-N interfaces (**Fig. S8**). By means of the extended transition-state method with natural orbitals for chemical valence[33] (ETS-NOCV), we further investigated this covalent interaction in $[CuL]^+$ and $[OC\text{-}CuL]^+$ (**Fig. S9**).For $[CuL]^+$, significant electron transfer from the ligand to Cu occurs, with the ligands acting as an “electron reservoir” for the Cu center. In the formation of the Cu-CO bond, two key electron transfer mechanisms were revealed: σ-donation and π-back-donation. Specifically, the C atom in CO donates electrons from its filled σ orbital to the Cu atom in the complex, forming a stable σ bond. Concurrently, the Cu atom in the complex donates electrons from its filled d orbital to the π* orbital of CO, a feedback mechanism that enhances the stability of the complex. Atomic dipole moment corrected Hirshfeld population (ADCH) charge population[34] was chosen for its ability to accurately describe transition metal systems, clearly demonstrating the charge transfer among the ligands, Cu atom and CO (**Fig. 2c**).

Besides, in the competitive adsorption of H_2O and CO, thermodynamically, $[Cu\text{-}Py]^+$ shows a stronger affinity for H_2O (ΔH_{H2O} = -154.15 kJ/mol) than that for CO. However, for $[Cu\text{-}bpy]^+$, the situation is reversed, i.e., ΔH_{H2O} = -108.09 kJ/mol *vs* ΔH_{CO} = -124.03 kJ/mol. Consequently, the $Cu\text{-}N_1$ coordination shows a clear signal of H_2O adsorption.

1.5 Effect of Additional Factors on Reaction Kinetics

The number of vibrational degrees of freedom and the collision cross-section play a crucial role in regulating energy dissipation during CO adsorption[35]. In systems with larger and more flexible ligands, enhanced intramolecular vibrational redistribution and broader collision cross-sections with inert cooling gases facilitate rapid energy relaxation, stabilize the adsorption complex, and improve apparent reactivity[36-38]. By contrast, $[Cu\text{-}CO]^+$ possesses only three vibrational modes and a linear geometry that restricts vibrational-rotational coupling, leading to strong energy localization and poor energy dissipation, despite its high binding energy—

explaining the inertness of $[Cu]^+$ toward CO. This mechanism also rationalizes the higher reactivity of $[Cu\text{-}bpy]^+$ over $[Cu\text{-}py]^+$ and $[Cu\text{-}Acr]^+$ over $[Cu\text{-}Qu]^+$, where increased vibrational flexibility and conjugation enable more efficient energy redistribution and stabilize the adsorption products.

1.6 Analysis of CO Stretching Vibrational Frequencies

A comparison of CO stretching frequencies across different cluster models shows that CO vibrational modes are sensitive to the coordination environment and electronic structure of the Cu center (**Table S6** and **Fig. S15**). In Cu^+, $Cu\text{-}N_1$ (excluding $[Cu\text{-}P\text{-}Py]^+$), and $Cu\text{-}N_2$ configurations, CO exhibits a blue shift[31, 39], whereas $Cu\text{-}N_3$, $Cu\text{-}N_4$, and P-doped systems show a red shift. As ligand conjugation and coordination number increase, the electron density on Cu increases, leading to a reduced blue shift in CO frequency (**Fig. S15**) and an increase in the C-O bond length (**Fig. S16**). This blue shift arises from the electronic configuration of the Cu(I) center, where the fully filled $3d^{10}$ orbitals result in weak Cu→CO π-backdonation. The Cu–CO bonding is primarily governed by Cu←CO σ-donation, which is considered to be weakly antibonding. The blue shift is rather due to an inductive effect of positively charged Cu atoms on the occupied orbitals of the CO ligand (**Table S7**), which become less polarized and thus shorter and stronger[40-41].

When Cu(I) coordinates with ligands, electron donation from the ligands enables Cu→CO π-backdonation, significantly reducing the blue shift in CO vibrational frequency compared to $[Cu\text{-}CO]^+$ (as detailed in **Table S7**). In $Cu\text{-}N_1$ configurations, increased ligand conjugation lowers the Cu center's positive charge, thereby diminishing the blue shift. $Cu\text{-}N_2$ shows even less blue shift and a longer C-O bond than $Cu\text{-}N_1$ configurations. Despite the relatively high Cu charge in $[Cu\text{-}phen]^+$ and $[Cu\text{-}bpy]^+$, CDA reveals relatively strong π-backdonation, likely due to the $Cu\text{-}N_2$ configuration facilitating efficient electron flow from ligand to CO. With further increases in coordination number and conjugation, as seen in $Cu\text{-}N_3$ and $Cu\text{-}N_4$, π-backdonation strengthens, leading to a clear red shift and further bond elongation. In $[Cu\text{-}P\text{-}Py]^+$, CO forms a stronger covalent bond with the P atom, receiving more electron density and producing an even greater red shift than in Cu-CO systems. Notably, CDA results for $[Cu\text{-}Py_2]^+$ and $[Cu\text{-}bpy_2]^+$ may be underestimated, as calculations were based on post-adsorption geometries and did not capture electron redistribution during adsorption-induced structural changes.

In addition, we calculated CO vibrational frequencies for the theoretically modeled $Cu\text{-}N_1$ and $Cu\text{-}N_2$ systems with extended conjugation (**Table S8**). Although the resulting changes in Cu center charge are minor and cause negligible variations in bonding strength (ΔE < 5 kJ/mol), these subtle electronic modulations still lead to red shifts in CO frequency due to enhanced π-back donation. A comparison of the data in **Table S8** with the $Cu\text{-}N_{1/2}$ data in **Table S6** shows that the direction of conjugation extension also influences the degree of frequency shift. We thus speculate that in practical catalytic systems, where support materials often exhibit stronger conjugation, CO vibrational red shifts may be more pronounced than those observed in our models. Nevertheless, the general trend of the redshift influenced by the N coordination number, conjugation size, and extension direction should remain valid.

Previous studies have primarily focused on $Cu\text{-}N_4$ systems, with some attention to $Cu\text{-}N_2$ and $Cu\text{-}N_3$ configurations. However, due to the weak CO adsorption tendency on $Cu\text{–}N_{3/4}$ sites during CO_2 reduction reactions (CO_2RR)[42-44], infrared spectroscopic data of CO remain scarce.

For example, Yang et al.[43] reports a CO adsorption energy of only –0.36 eV on Cu-N_3 single-atom catalysts (SACs), indicating that CO desorption is facile. Similarly, Guo et al.[44] reported that Cu-N_3 could not effectively adsorb *CO, as evidenced by the absence of corresponding Diffuse Reflectance Infrared Fourier-Transform Spectroscopy (DRIFTS) signals. Moreover, Wu et al.[45] observed no C-O stretching peak for Cu-N_4, consistent with its unfavorable adsorption enthalpy of +0.58 eV, whereas Cu-N_2 exhibits stronger CO binding (–1.79 eV) and a red-shifted C-O stretching frequency at 2025 cm^{-1}. This trend in Cu-N_2 system agrees with our findings that increased ligand conjugation and electron density at the Cu center enhances Cu→CO π-backdonation, leading to further red shifts in CO vibrational frequencies (**Table S8** and **Fig. S15**). Additionally, Nielsen et al.[45] showed that higher electron density on Cu (from Cu^+ to Cu^0 and then to Cu^-) systematically lowers CO stretching frequencies[46]. Together, these studies provide valuable experimental benchmarks that support and enrich the interpretations in our work.

2. Supplementary Figures

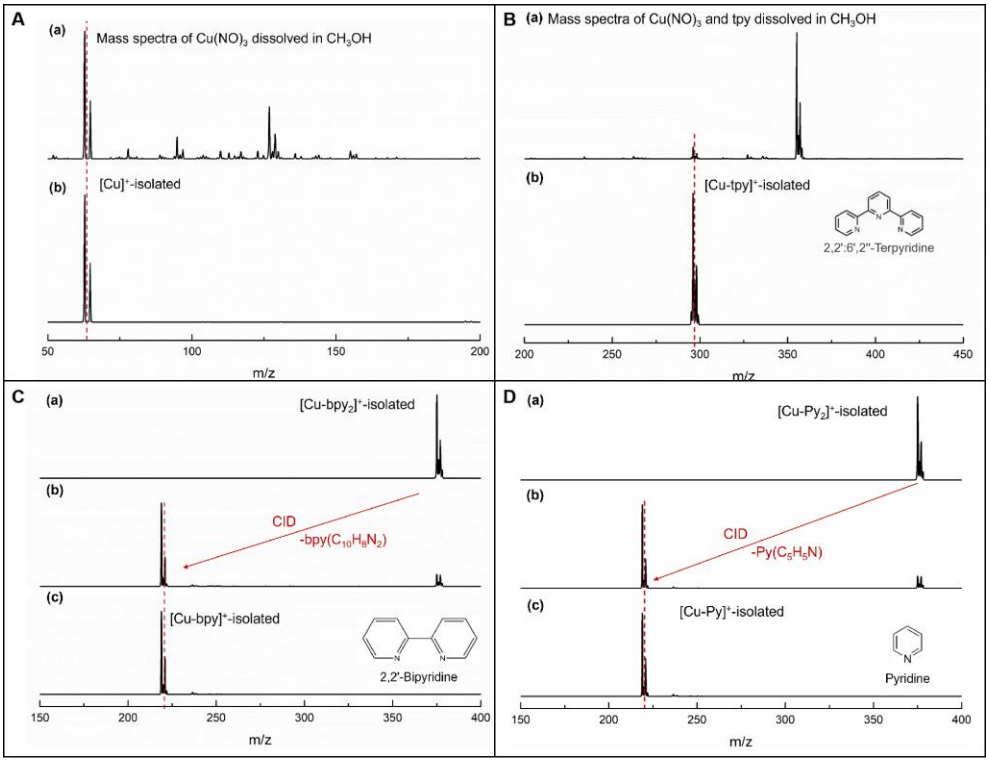

Fig. S1. Mass spectra of isolated and collision induced dissociation process of $[Cu]^+$ and $[CuL]^+$ **(A)** $[Cu]^+$; **(B)** $[Cu\text{-}tpy]^+$; **(C)** $[Cu\text{-}bpy_n]^+$ and **(D)** $[Cu\text{-}Py_n]^+$ (n = 1-2).

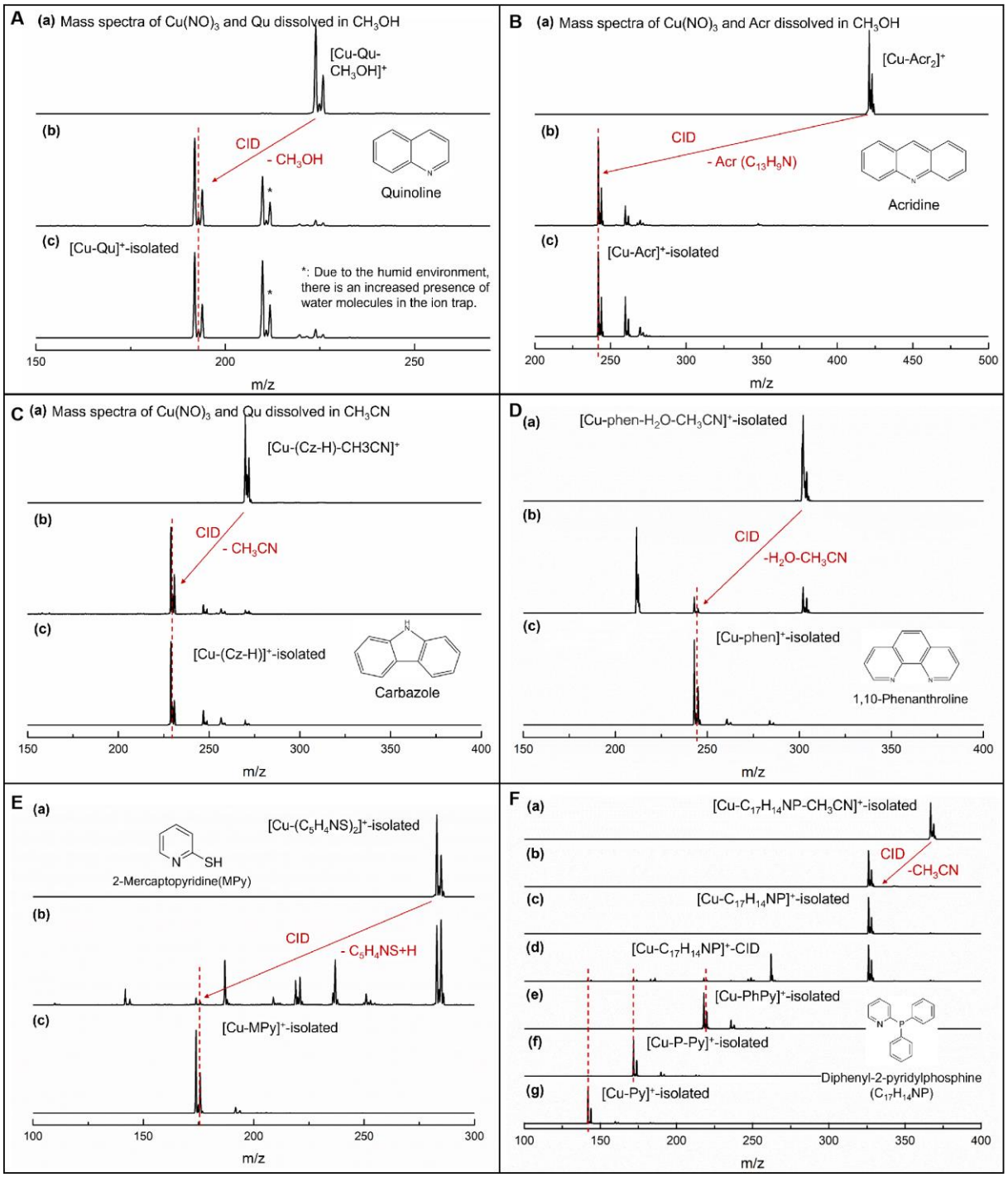

Fig. S2. Mass spectra of collision induced dissociation process of $[CuL]^+$ **(A)** $[Cu\text{-}Qu]^+$; **(B)** $[Cu\text{-}Acr]^+$; **(C)** $[Cu\text{-}Cz]^+$; **(D)** $[Cu\text{-}phen]^+$; **(E)** $[Cu\text{-}Mpy]^+$ and **(F)** $[Cu\text{-}P\text{-}Py]^+$ and $[Cu\text{-}PhPy]^+$, where $[Cu\text{-}Cz]^+$ complex undergoes a loss of the hydrogen on the pyrrole N during its formation, better simulating the actual catalytic environment.

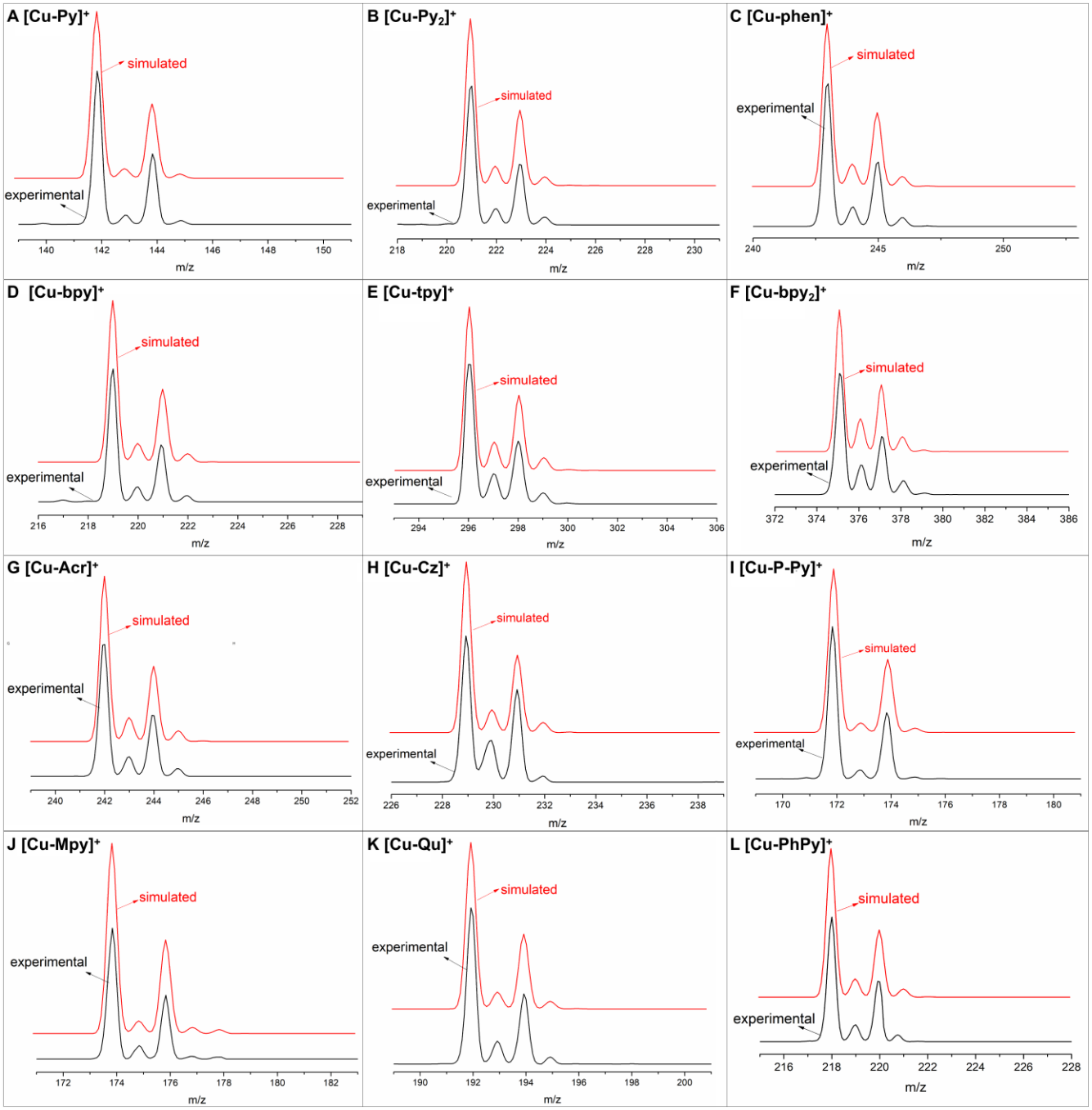

Fig. S3. Isotopic distributions of the experimental and the simulated $[CuL]^+$.

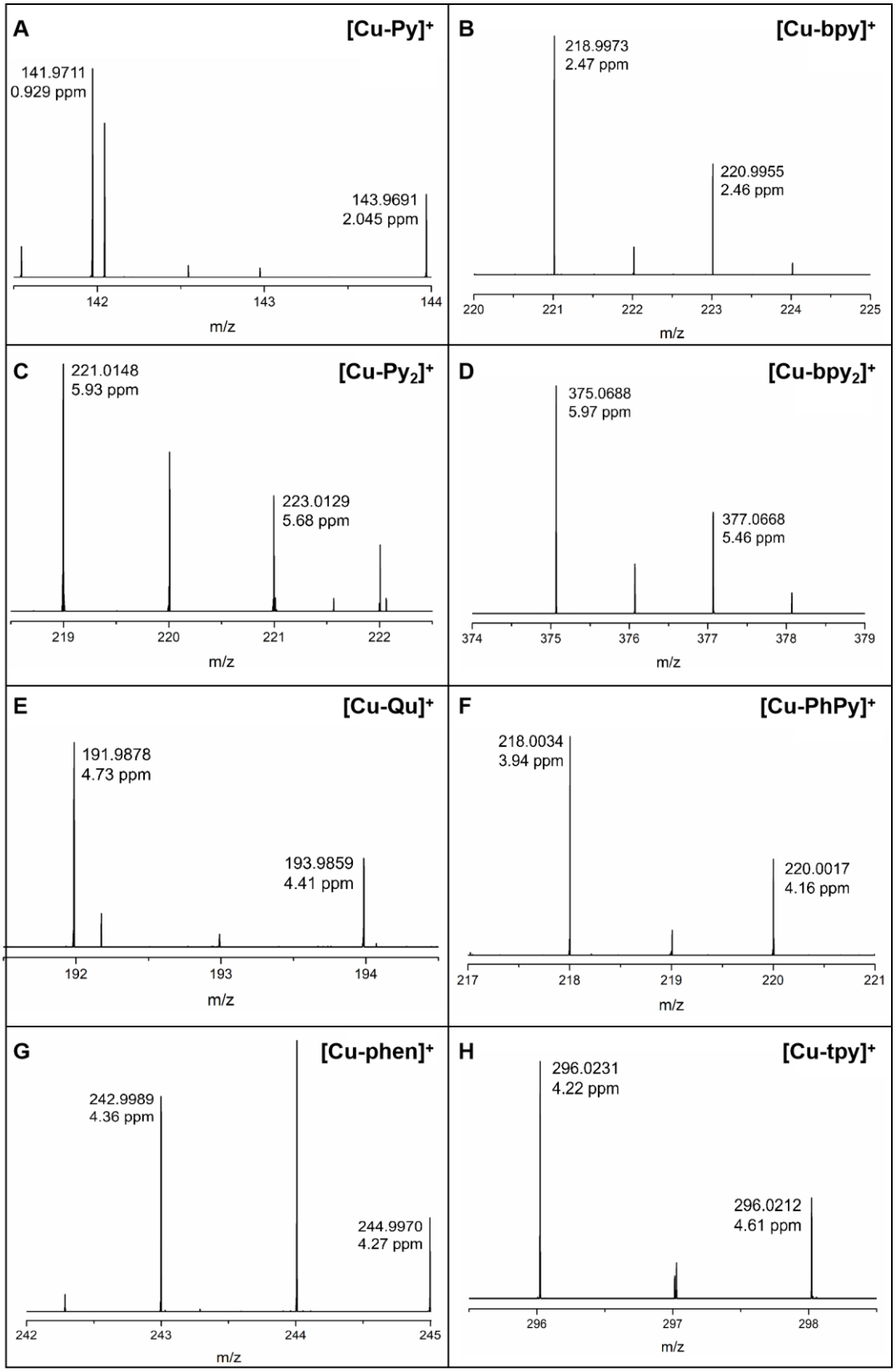

Fig. S4. Mass spectra of $[CuL]^+$ acquired using a Q Exactive (QE) mass spectrometer with a resolution of 140,000 to accurately determine the elemental composition and quantity, including Cu, N, C, P, S, and others.

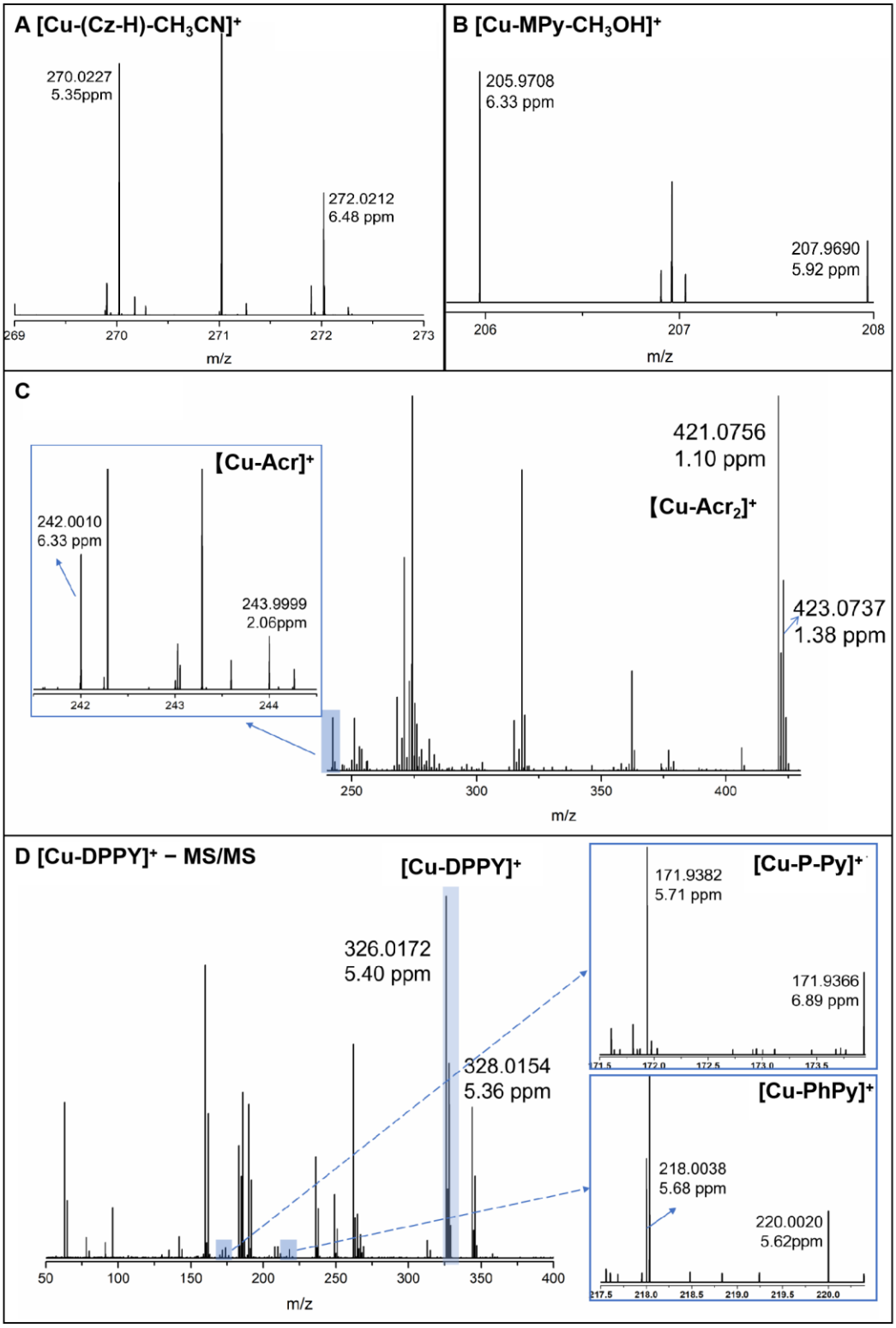

Fig. S5. Mass spectra of parent ions of $[CuL]^+$ acquired using a Q Exactive mass spectrometer with a resolution of 140,000 to accurately determine the elemental composition and quantity, including Cu, N, C, P, S, and others. Under the QE conditions, the signals for Cu adsorbing only Cz or MPy were not prominent. Therefore, the displayed results correspond to the target ion adsorbing solvent molecules.

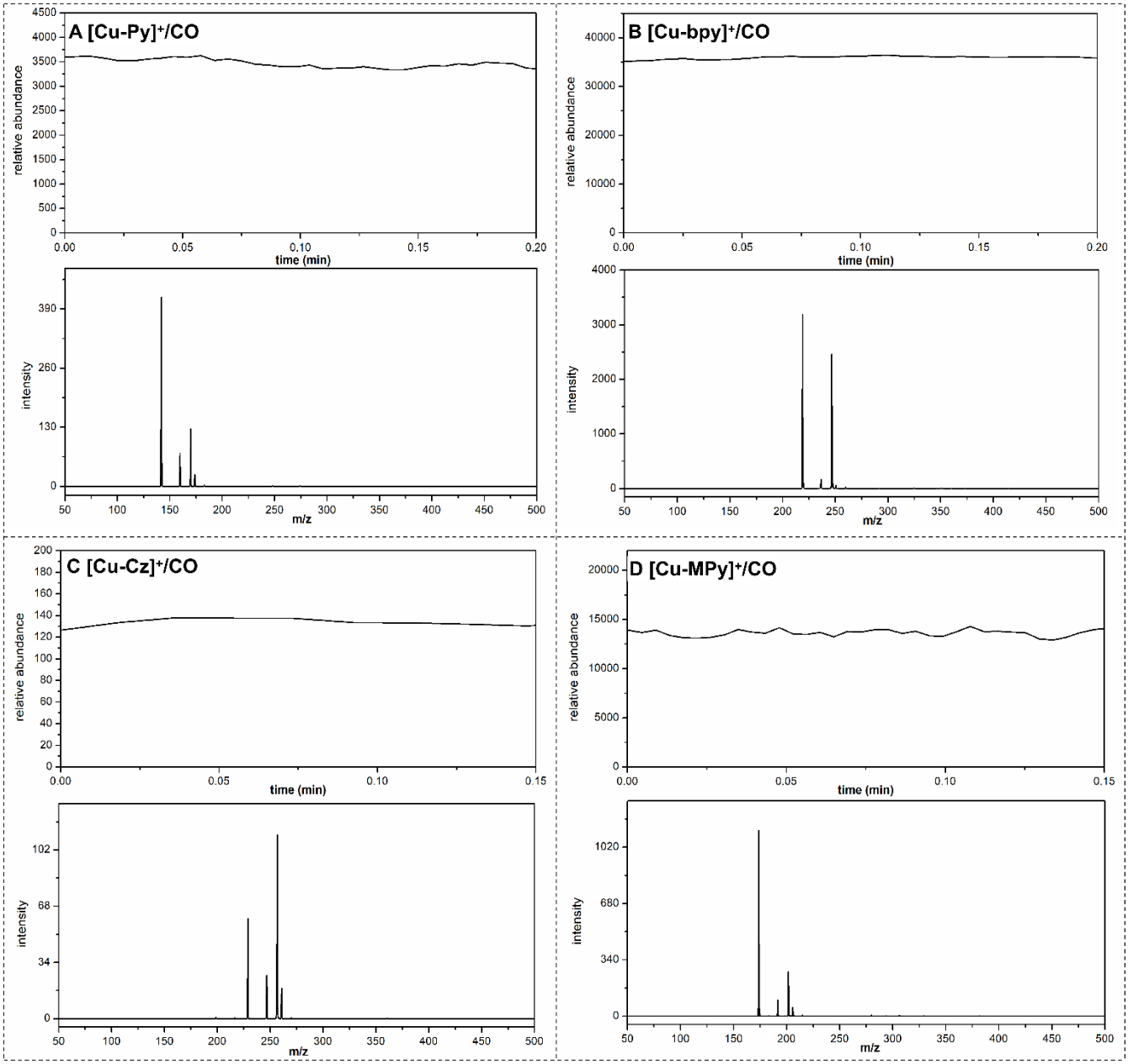

Fig. S6a. Ion current profile of $[CuL]^+$ and their mass spectra after 20 ms CO exposure. The distinct peaks are as follows: $[CuL]^+$, $[CuL\text{-}H_2O]^+$, $[CuL\text{-}CO]^+$, and $[CuL\text{-}CH_3OH]^+$. The absence of fragment ion peaks of $[CuL]^+$ and other extraneous signals, along with the stable ion current, confirms that the cluster ions are inherently stable and do not undergo fragmentation upon CO exposure.

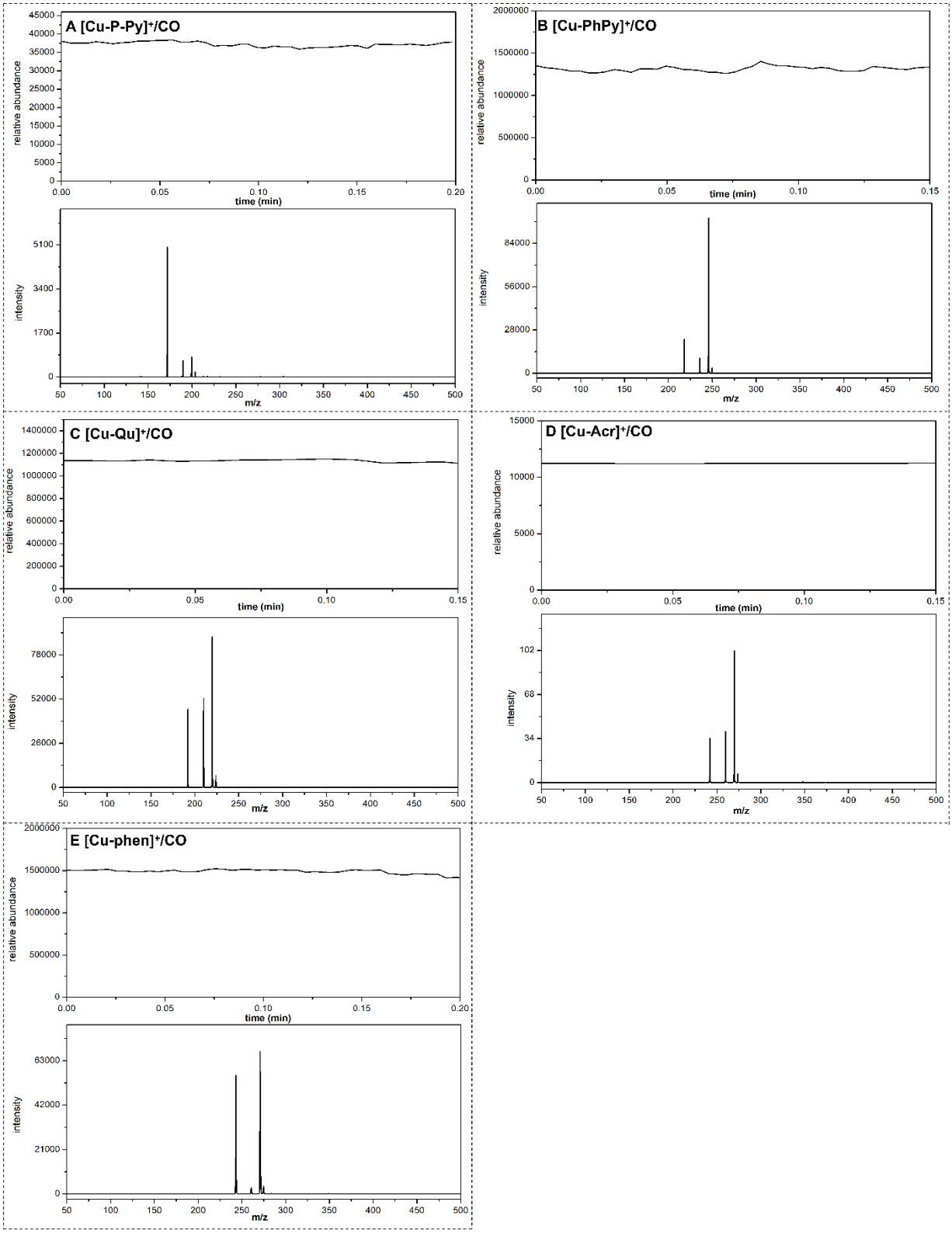

Fig. S6b. Ion current profile of $[CuL]^+$ and their mass spectra after 20 ms CO exposure. The distinct peaks as follows: $[CuL]^+$, $[CuL\text{-}H_2O]^+$, $[CuL\text{-}CO]^+$, and $[CuL\text{-}CH_3OH]^+$.

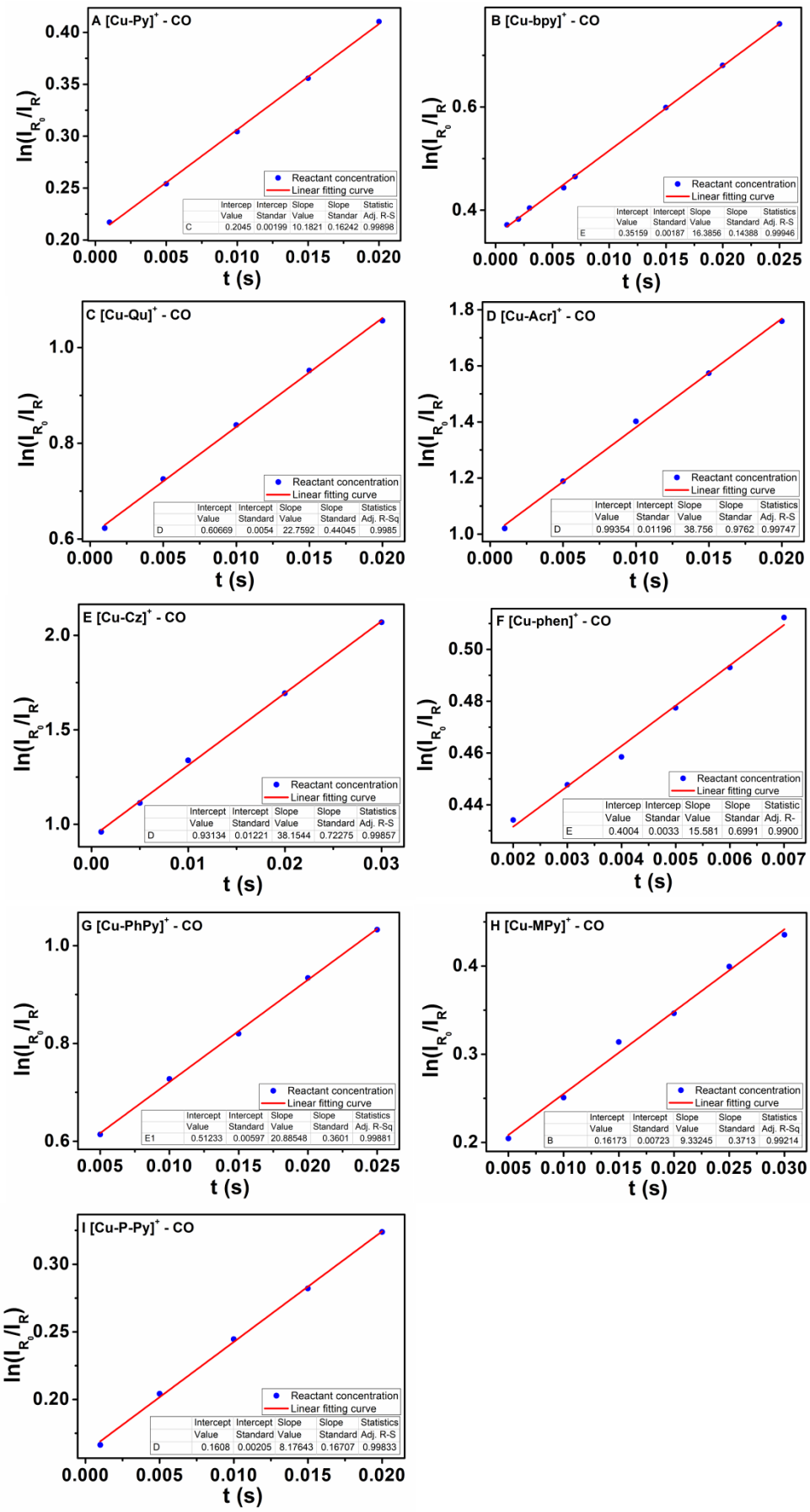

Fig. S7. Details of the calculation of the rate constants (*k*).

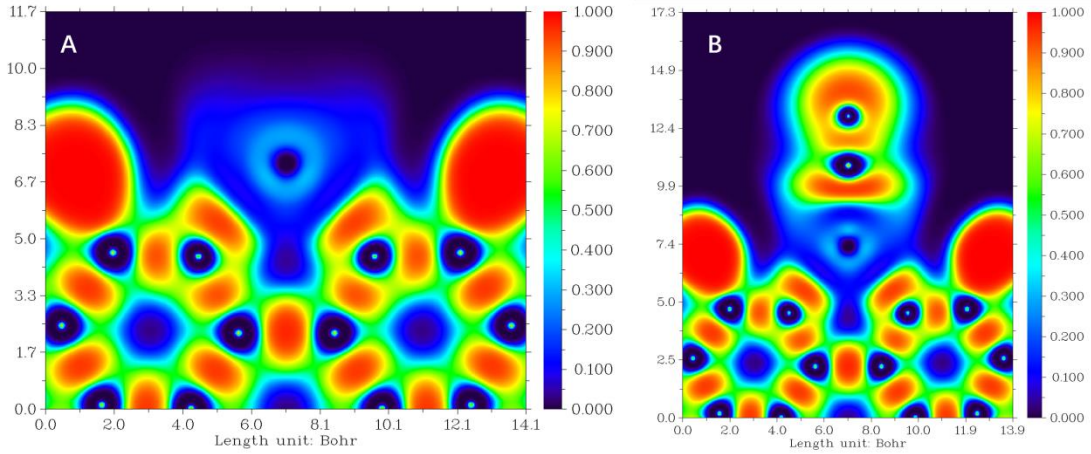

Fig. S8. Color-filled maps of valence electron density of **(A)** [Cu-bpy]$^+$ and **(B)** [OC-Cu-bpy]$^+$.

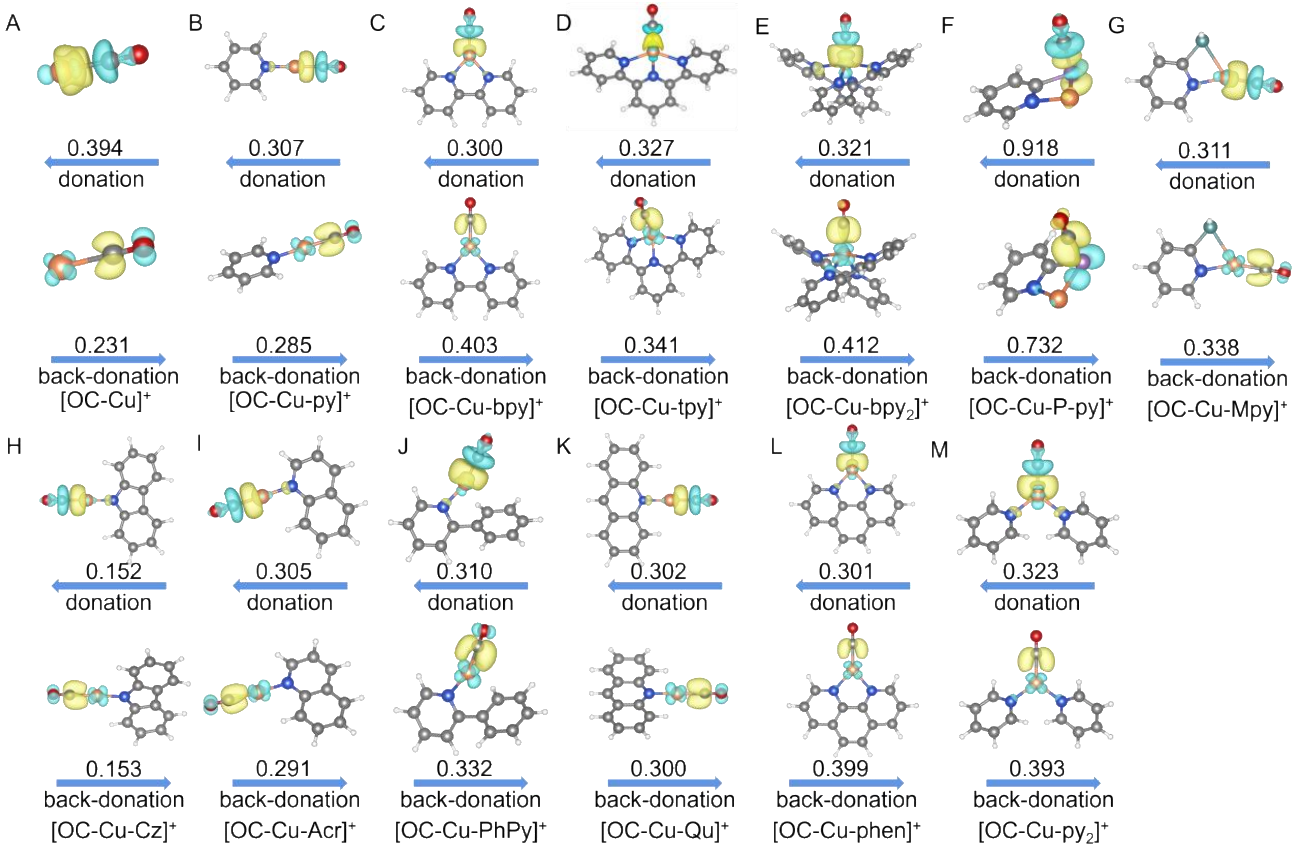

Fig. S9. ETS-NOCV description of the electron flow in the OC-CuL bonds in [OC-CuL]$^+$, and shape of the corresponding deformation density for the representative pairs of NOCVs, with blue regions representing areas of electron depletion (negative values), and yellow regions representing areas of electron accumulation (positive values).

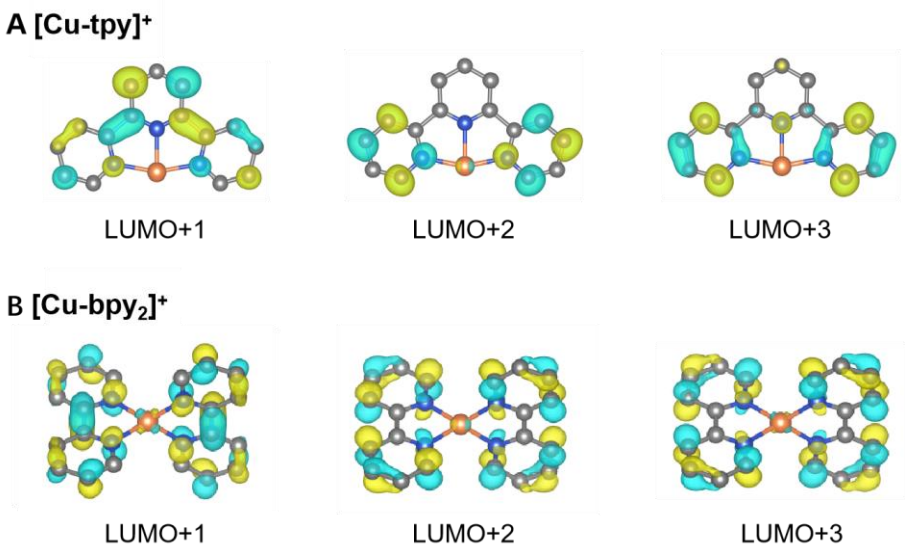

Fig. S10. Frontier orbital structures of **(A)** [Cu-tpy]$^+$ and **(B)** [Cu-bpy$_2$]$^+$, including LUMO+n (*n* = 1-3)

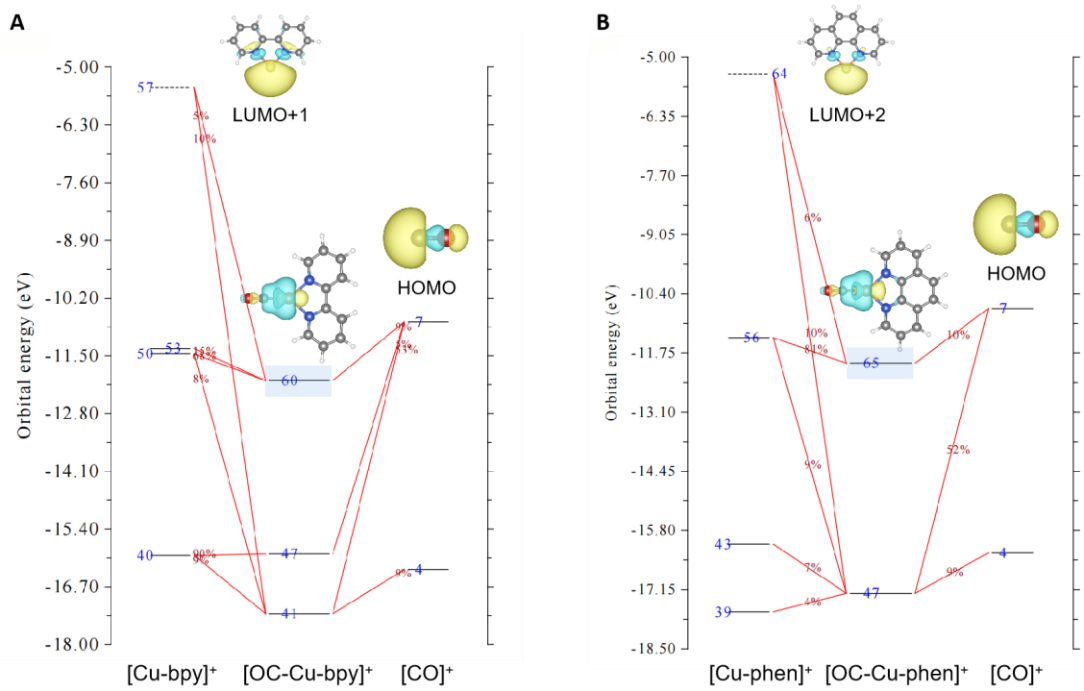

Fig. S11. Partial orbital interaction diagrams for **(A)** [Cu-bpy]$^+$ and **(B)** [Cu-phen]$^+$. Vertical axis shows MO energies in eV. Solid and dashed bars correspond to occupied and virtual MOs, respectively Some MOs are plotted as isosurface graphs with an isovalue of 0.03. The numbers marked beside the red lines indicate the contribution from the fragmental MO to the [CuL]$^+$ MOs. For clarity, only the orbitals that contribute to the electron transfer from CO to [CuL]$^+$ are shown, with the bonding orbitals marked as the dominant contributors.

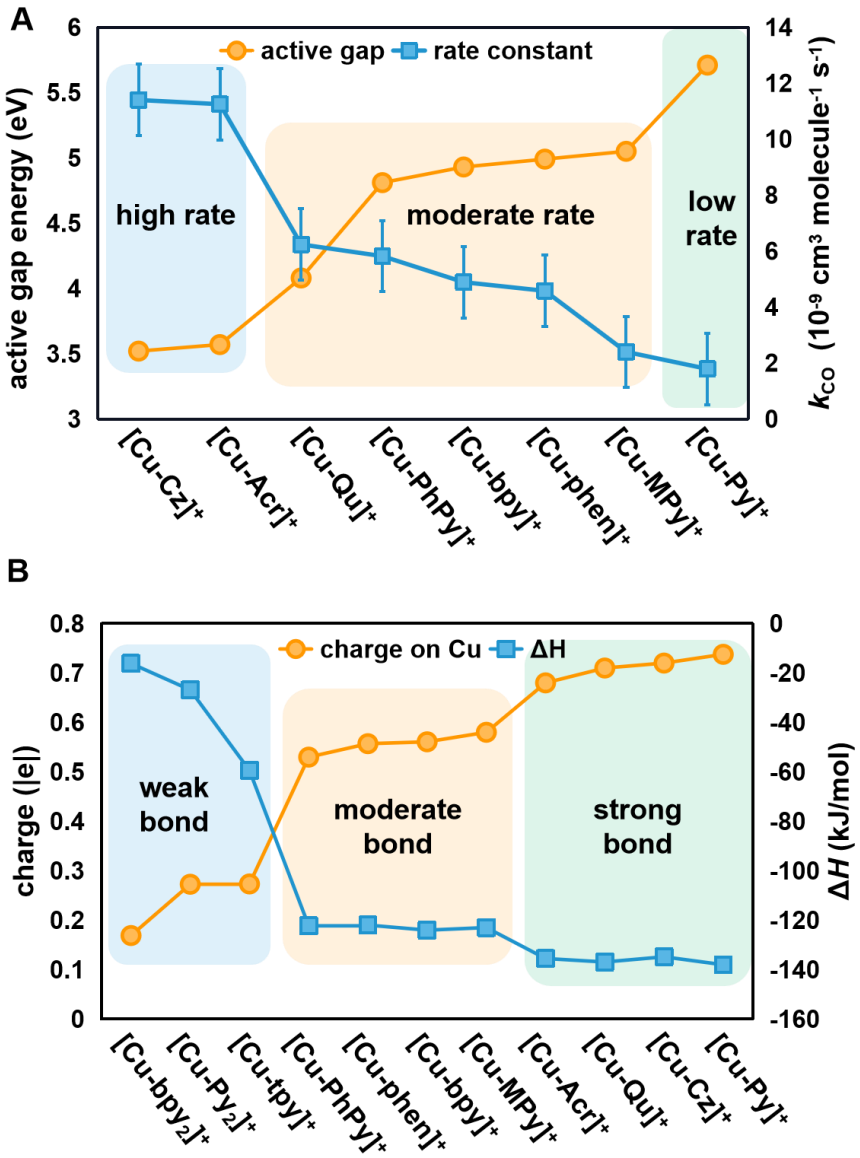

Fig. S12. (A) The relationship between the active gap and the experimental adsorption rate of CO, with an error margin of about 30%; **(B)** the variation of exothermicity with respect to the charge on Cu atom of $[CuL]^+$.

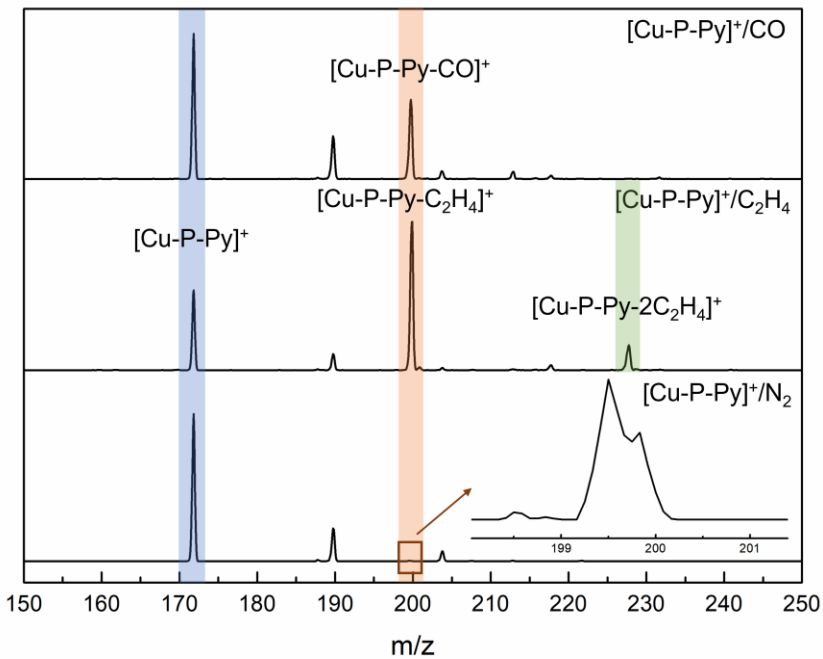

Fig. S13. ESI mass spectra for the adsorption of $CO/C_2H_4/N_2$ with mass-selected $[Cu\text{-}P\text{-}Py]^+$. Reaction time is 30 ms.

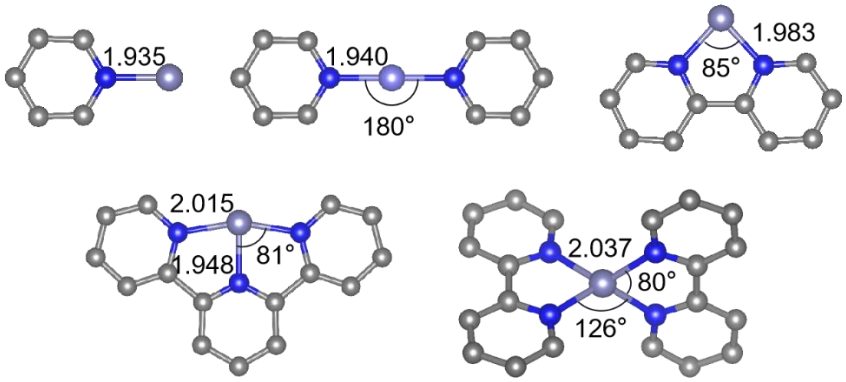

Fig. S14. Structural details of the $[CoL]^+$ cluster models. Unlike $[CuL]^+$, the lowest-energy structures of the $[CoL]^+$ complexes adopt a triplet state at PBE0-D3(BJ)/def2tzvpp level[28-29].

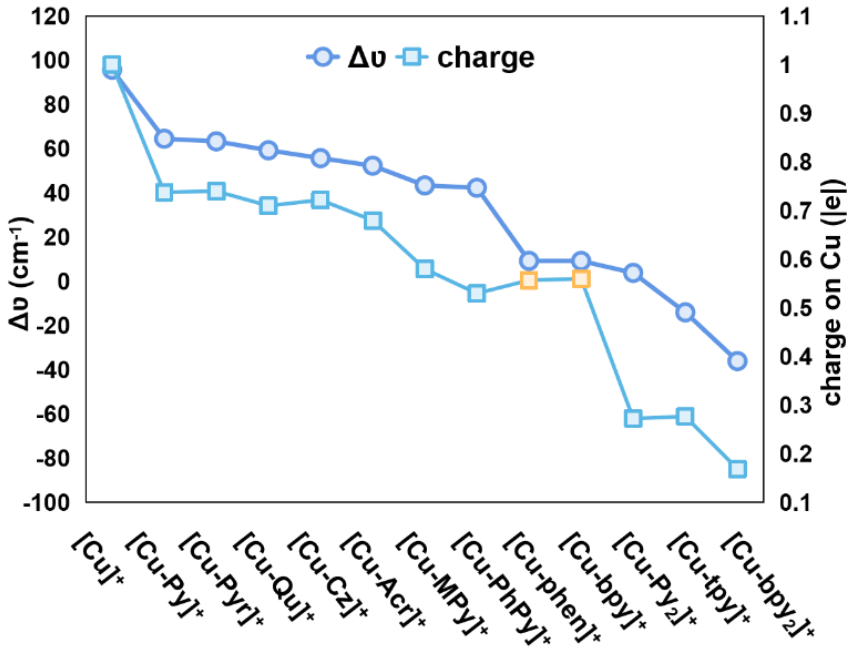

Fig. S15. The correlation between the frequency shift of CO and the change on Cu; data points deviating from the general trend are marked in yellow.

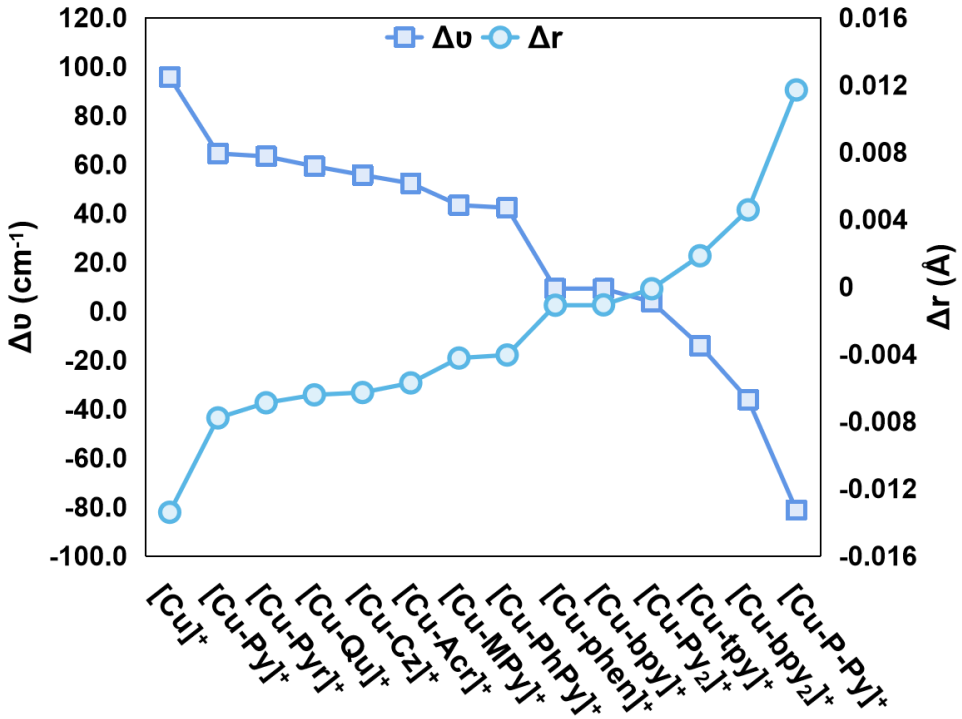

Fig. S16. The correlation between the frequency shift of C-O and the change in C-O bond length.

3. Supplementary Tables

Table S1. Details of the calculation of the rate constants (*k*).

Model clusters	k'_T (s^{-1})	Adjusted R-Squared	* k_T (10^{-9} cm^3 /(molecule•s)	k_{CO}/k_T	k_{CO} 1.00×10^{-9} (±30%) cm^3 /(molecule•s)
$[Cu\text{-}Py]^+$	10.18	0.99778	3.14	0.58	1.81
$[Cu\text{-}bpy]^+$	16.39	0.99946	5.06	0.98	4.96
$[Cu\text{-}Qu]^+$	22.76	0.99850	7.03	0.90	6.32
$[Cu\text{-}Acr]^+$	38.76	0.99747	11.97	0.95	11.37
$[Cu\text{-}Cz]^+$	38.15	0.99747	11.78	0.97	11.46
$[Cu\text{-}phen]^+$	15.58	0.99001	4.81	0.97	4.66
$[Cu\text{-}PhPy]^+$	20.89	0.99881	6.45	0.92	5.92
$[Cu\text{-}MPy]^+$	9.33	0.99214	2.88	0.84	2.42
$[Cu\text{-}P\text{-}Py]^+$	8.18	0.99833	2.53	0.80	2.02

Table S2. Energy decomposition analysis (EDA) of the interactions between Cu atom and the ligands in $[CuL]^+$. Numbers in parentheses are the percentage of electrostatic/orbital interactions in the total attractive forces.

Complexes	ΔE_els kcal/mol	ΔE_x kcal/mol	ΔE_xrep kcal/mol	ΔE_orb kcal/mol	ΔE_c kcal/mol	Total kcal/mol
$[Cu\text{-}Py]^+$	−67.7(49%)	−38.6	89.7	−62.4 (25%)	−18.2	−68.9
$[Cu\text{-}bpy]^+$	−138.3(49%)	−55.5	120.8	−68.8(25%)	−17.4	−103.7
$[Cu\text{-}tpy]^+$	−172.8(48%)	−69.00	148.7	−91.6(26%)	−23.1	−138.7
$[Cu\text{-}bpy_2]^+$	−215.4(48%)	−88.1	187.7	−115.1(26%)	−30.0	−172.8
$[Cu\text{-}phen]^+$	−135.6(49%)	−54.4	117.9	−69.4(25%)	−17.2	−104.2
$[Cu\text{-}Py_2]^+$	−183.4(48%)	−76.8	173.5	−100.3(26%)	−21.7	−131.8
$[Cu\text{-}PhPy]^+$	−97.4(43%)	−45.3	96.1	−67.5(30%)	−16.6	−85.5
$[Cu\text{-}Qu]^+$	−96.6(48%)	−40.0	89.46	−53.9(27%)	−12.2	−73.2
$[Cu\text{-}Acr]^+$	−98.6(46%)	−41.6	92.91	−58.9(28%)	−13.4	−78.0
$[Cu\text{-}Cz]^+$	−102.4(46%)	−42.3	95.60	−57.4(27%)	−12.3	−76.5
$[Cu\text{-}MPy]^+$	−92.0(45%)	−40.5	84.30	−57.5(28%)	−14.2	−79.5
$[Cu\text{-}P\text{-}Py]^+$	−28.7 (15%)	−29.2	97.50	−100.2(63%)	−12.6	−100.9

Table S3. Energy Decomposition Analysis of the Interactions between $[CuL]^+$ and CO in $[OC\text{-}CuL]^+$. Numbers in Parentheses are the Percentage of Electrostatic/orbital Interactions in the Total Attractive Interaction.

Complexes	ΔE_els kcal/mol	ΔE_x kcal/mol	ΔE_xrep kcal/mol	ΔE_orb kcal/mol	ΔE_c kcal/mol	Total kcal/mol
[**OC**-Cu]$^+$	−69.9(44%)	−38.7	82.8	−41.9(26%)	−9.7	−38.7
[**OC**-Cu-Py]$^+$	−73.3(44%)	−40.7	84.2	−41.1(24%)	−10.9	−41.0
[**OC**-Cu-Pyr]$^+$	−79.4(44%)	−46.5	97.24	-43.6(24.0%)	-12.1	-37.85
[**OC**-Cu-bpy]$^+$	−86.9(43%)	−52.1	109.1	−48.2(24%)	−13.4	−39.3
[**OC**-Cu-tpy]$^+$	−91.4(42%)	−59.1	127.3	−42.3(23%)	−15.5	−29.6
[**OC**-Cu-bpy$_2$]$^+$	−92.0(42%)	−61.0	130.6	−49.6(26%)	−17.1	−28.1
[**OC**-Cu-phen]$^+$	−86.5(43%)	−52.0	109.1	−47.8(24%)	−13.3	−38.5
[**OC**-Cu-Py$_2$]$^+$	−86.5(43%)	−54.2	115.4	−47.8 (24%)	−14.0	−32.8
[**OC**-Cu-PhPy]$^+$	−79.7(44%)	−46.7	97.8	−43.5(24%)	−12.6	−37.9
[**OC**-Cu-Qu]$^+$	−74.1(44%)	−41.6	86.0	−41.3 (25%)	−11.2	−40.5
[**OC**-Cu-Acr]$^+$	−75.1(46%)	−42.6	88.3	−41.6 (28%)	−11.6	−39.9
[**OC**-Cu-Cz]$^+$	−73.5 (44%)	−41.1	85.3	−41.1(25%)	−11.1	−40.4
[**OC**-Cu-MPy]$^+$	−79.4(44%)	−46.5	97.2	−43.6(24%)	−12.1	−37.9
[**OC**-Cu-P-Py]$^+$	−132.5(29%)	−107.5	295.0	−195.3(43%)	−23.2	−56.0

Table S4. Mayer Bond Order of Cu-N Bond in $[CuL]^+$ and Cu-CO Bond in $[OC\text{-}CuL]^+$.

Complexes	Cu-N Mayer bond order	Complexes	Cu-C Mayer bond order
$[Cu]^+$	--	[**OC**-Cu]$^+$	0.96
$[Cu\text{-}Py]^+$	0.82	[**OC**-Cu-Py]$^+$	0.76
$[Cu\text{-}bpy]^+$	0.58, 0.58	[**OC**-Cu-bpy]$^+$	0.88
$[Cu\text{-}tpy]^+$	0.51, 0.35, 0.51	[**OC**-Cu-tpy]$^+$	0.82
$[Cu\text{-}bpy_2]^+$	0.43, 0.43,0.43, 0.43	[**OC**-Cu-bpy$_2$]$^+$	0.83
$[Cu\text{-}phen]^+$	0.60, 0.60	[**OC**-Cu-phen]$^+$	0.91
$[Cu\text{-}Py_2]^+$	0.71, 0.71	[**OC**-Cu-Py$_2$]$^+$	0.87
$[Cu\text{-}PhPy]^+$	0.62 (Cu-C:0.30)	[**OC**-Cu-PhPy]$^+$	0.81
$[Cu\text{-}Qu]^+$	0.87	[**OC**-Cu-Qu]$^+$	0.76
$[Cu\text{-}Acr]^+$	0.92	[**OC**-Cu-Acr]$^+$	0.75
$[Cu\text{-}Cz]^+$	0.91	[**OC**-Cu-Cz]$^+$	0.75
$[Cu\text{-}MPy]^+$	0.57 (Cu-S:0.54)	[**OC**-Cu-MPy]$^+$	0.84
$[Cu\text{-}P\text{-}Py]^+$	0.34 (Cu-P:1.12)	[**OC**-Cu-P-Py]$^+$	Cu-P:1.34

Table S5. DFT Calculated Values of Gibbs Free Energy (*ΔG*), Charge on Cu of $[CuL]^+$, Enthalpy (*ΔH*), Scaled C-O Frequencies, and Active Gap for the Reaction of $[CuL]^+$ with CO, along with the Experimental Rate Constants (k_{CO}).

Model clusters	*ΔG* kJ/mol	Charge |e|	*ΔH* kJ/mol	Scaled υ(C-O) (cm^{-1})	Active Gap eV	k_{CO} 1.00×10^{-9} (±30%) cm^3 $molecule^{-1}$ s^{-1}
$[Cu]^+$	−78.88	1.00	−124.37	2219.5	5.81	−−
$[Cu\text{-}Py]^+$	−97.56	0.74	−138.02	2188.3	5.71	1.81
$[Cu\text{-}bpy]^+$	−80.94	0.56	−124.03	2133.0	4.93	4.96
$[Cu\text{-}tpy]^+$	−27.01	0.28	−59.41	2109.7	−−	−−
$[Cu\text{-}bpy_2]^+$	22.00	0.17	−16.94	2087.7	−−	−−
$[Cu\text{-}Qu]^+$	−96.38	0.71	−136.91	2183.0	4.08	6.32
$[Cu\text{-}Acr]^+$	−94.43	0.68	−135.50	2176.1	3.57	11.37
$[Cu\text{-}Cz]^+$	−94.13	0.72	−134.81	2179.5	3.52	11.46
$[Cu\text{-}phen]^+$	−81.01	0.56	−121.97	2133.0	4.99	4.66
$[Cu\text{-}Py_2]^+$	1.78	0.27	−26.84	2127.6	−−	−−
$[Cu\text{-}PhPy]^+$	−83.12	0.53	−122.27	2166.1	4.81	5.92
$[Cu\text{-}MPy]^+$	−83.43	0.58	−122.98	2167.1	5.05	2.42
$[Cu\text{-}P\text{-}Py]^+$	−123.15	−−	−167.94	2042.5	4.84	2.02

Table S6. Calculated and Scaled C-O Frequencies, C-O Bond Lengths, C-O Stretching Frequency and Bond Length Shift Relative to Free CO, Charges on Cu Centers in Cluster Models.

Cu-N_x	Cluster model	υ(C-O) (cm^{-1})	Scaled υ[a] (cm^{-1})	Δυ[b] (cm^{-1})	r(C-O) (Å)	Δr[c] (Å)	Charge (|e|)
—	**CO**	2214.5	2123.7	—	1.1234	—	—
Cu-N_0	[**OC**-Cu]$^+$	2314.4	2219.5	95.7	1.1100	−0.0134	1.00
	[**OC**-Cu-Py]$^+$	2281.8	2188.3	64.5	1.1156	−0.0078	0.74
	[**OC**-Cu-Pyr]$^+$	2280.6	2187.1	63.3	1.1165	−0.0069	0.74
	[**OC**-Cu-Qu]$^+$	2276.4	2183.0	59.3	1.1170	−0.0064	0.71
Cu-N_1	[**OC**-Cu-Cz]$^+$	2272.7	2179.5	55.7	1.1171	−0.0063	0.72
	[**OC**-Cu-Acr]$^+$	2269.1	2176.1	52.3	1.1177	−0.0057	0.68
	[**OC**-Cu-MPy]$^+$	2259.8	2167.1	43.4	1.1192	−0.0042	0.58
	[**OC**-Cu-PhPy]$^+$	2258.7	2166.1	42.3	1.1194	−0.0040	0.53
	[**OC**-Cu-phen]$^+$	2224.2	2133.0	9.3	1.1223	−0.0011	0.56
Cu-N_2	[**OC**-Cu-bpy]$^+$	2224.2	2133.0	9.3	1.1223	−0.0011	0.56
	[**OC**-Cu-Py_2]$^+$	2218.5	2127.6	3.9	1.1233	−0.0001	0.27
Cu-N_3	[**OC**-Cu-tpy]$^+$	2199.9	2109.7	−14.0	1.1253	0.0019	0.28
Cu-N_4	[**OC**-Cu-bpy_2]$^+$	2176.9	2087.7	−36.0	1.1280	0.0046	0.17
Cu-N_1	[**OC**-Cu-P-Py]$^+$	2129.8	2042.5	−81.3	1.1351	0.0117	—

[a]: Scale factor value of B3LYP/def2-TZVP is 0.959 according to Database of Frequency Scale Factors for Electronic Model Chemistries.

[b]:Frequency shift relative to free CO based on scaled values.

[c]: C-O bond length shift relative to free CO based on calculated values.

Table S7. C-O Stretching Frequency Shift, Analysis of Cu←CO σ-Donation and Cu→CO π-Back Donation Electron Counts With Its Percentage Contribution to the Total Electron Transfer, and Classical Electrostatic Interaction Energy (E_els) along with its Relative Contribution to the Total Attractive Interactions in the Cluster Models

Cu-N_x	Cluster model	Δυ (cm^{-1})	σ-donation (e)	π-back donation (e)	E_els (kcal/mol)
Cu-N_0	[**OC**-Cu]$^+$	95.7	0.3209	0.0484 (13.11%)	−69.94 (43.66%)
	[**OC**-Cu-py]$^+$	64.5	0.3207	0.0621 (16.23%)	−73.27 (44.16%)
	[**OC**-Cu-pyr]$^+$	63.3	0.3200	0.0647 (16.82%)	−73.37 (44.17%)
	[**OC**-Cu-Qu]$^+$	59.3	0.3198	0.0634 (16.54%)	−74.08 (44.07%)
Cu-N_1	[**OC**-Cu-Cz]$^+$	55.7	0.3198	0.0626 (16.37%)	−73.54 (44.07%)
	[**OC**-Cu-Acr]$^+$	52.3	0.3185	0.0646 (16.85%)	−75.05 (43.93%)
	[**OC**-Cu-MPy]$^+$	43.4	0.3180	0.0703 (18.94%)	−79.40 (43.73%)
	[**OC**-Cu-PhPy]$^+$	42.3	0.3137	0.0733 (18.85%)	−79.65 (43.65%)
	[**OC**-Cu-phen]$^+$	9.3	0.3160	0.0734 (21.81%)	−86.54 (43.33%)
Cu-N_2	[**OC**-Cu-bpy]$^+$	9.3	0.3091	0.0862 (22.39%)	−86.87 (43.32%)
	[**OC**-Cu-Py_2]$^+$	3.9	0.3097	0.0894 (19.10%)	−86.50 (42.73%)
Cu-N_3	[**OC**-Cu-tpy]$^+$	−14.0	0.3017	0.0712 (20.20%)	−91.44 (42.31%)
Cu-N_4	[**OC**-Cu-bpy_2]$^+$	−36.0	0.2906	0.0735 (20.36%)	−92.02 (41.86%)
Cu-N_1	[**OC**-Cu-P-Py]$^+$	−81.3	0.3004	0.0768 (33.87%)	−132.49 (28.90%)

Table S8. Scaled C-O Stretching Frequencies, C-O Bond Lengths, Frequency and C-O bond Length Shift Relative to Free CO, Charges on Cu Centers in the Theoretical Cluster Models with Conjugation Extension.

Cluster model	υ(C-O) (cm^{-1})	Scaled υ (cm^{-1})	Δυ (cm^{-1})	r(C-O) (Å)	Δr (Å)	Charge (|e|)
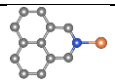	2276.6	2183.2	59.5	1.1170	−0.0064	0.72
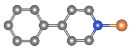	2276.2	2182.9	59.2	1.1170	−0.0064	0.73
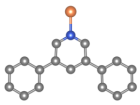	2276.1	2182.8	59.1	1.1171	−0.0063	0.72
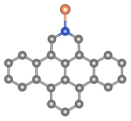	2270.2	2177.2	53.4	1.1175	-0.0059	0.74
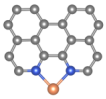	2220.6	2129.6	5.8	1.1235	0.0001	0.55
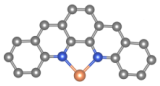	2210.8	2120.2	−3.5	1.1245	0.0011	0.51
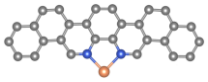	2209.9	2119.3	−4.4	1.1248	0.0014	0.53

Table S9. The Structure Diagrams of [Cu-Py]$^+$, [Cu-Pyr]$^+$, [Cu-Acr]$^+$and [Cu-Cz]$^+$, along with their Active Gap Values, the Charge on the Cu Center, and *ΔH* for CO Adsorption. Hydrogen Atoms were Omitted for Clarity.

Complexes	Structure diagram	*ΔH* (kJ/mol)	Charge (|e|)	Active gap (eV)
[Cu-Py]$^+$	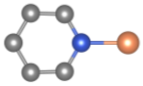	−138.02	0.74	5.71
[Cu-Pyr]$^+$ (simulated)	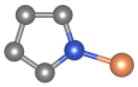	−136.12	0.74	5.15
[Cu-Acr]$^+$	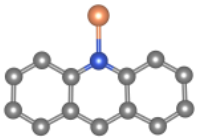	−122.32	0.68	3.57
[Cu-Cz]$^+$	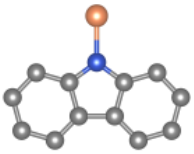	−136.17	0.72	3.52

Table S10. The Structure Diagrams of Cu-N_1 (including $[Cu\text{-}Py]^+$ and Theoretical Models), along with their Active Gap Values and the Charge on the Cu Center. Hydrogen AToms were Omitted for CLarity.

Structure diagram	Charge (|e|)	Active gap (eV)
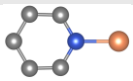 **$[Cu\text{-}Py]^+$**	0.74	5.71
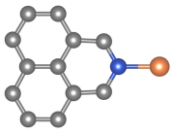 **Theoretical model 1**	0.72	5.10
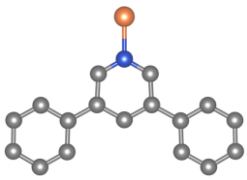 **Theoretical model 2**	0.72	5.55
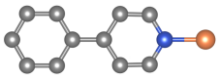 **Theoretical model 3**	0.73	5.67
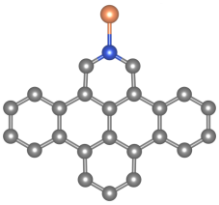 **Theoretical model 4**	0.74	5.75

Table S11. The Structure Diagrams of Cu-N_2 Structure with Ligands of Different Sizes (including $[Cu\text{-}bpy]^+$, $[Cu\text{-}phen]^+$ and Theoretical Models), along with their Active Gap Values, the Charge on the Cu Center, and *Δ*H for CO Adsorption. Hydrogen Atoms were Omitted for Clarity.

Structure diagram	*ΔH* (kJ/mol)	Charge (|e|)	Active gap (eV)
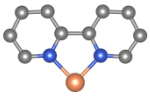 **$[Cu\text{-}bpy]^+$**	−124.03	0.56	4.93
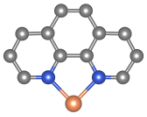 **$[Cu\text{-}phen]^+$**	−121.97	0.56	4.99
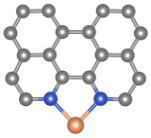 **Theoretical model 1**	−122.59	0.55	4.91
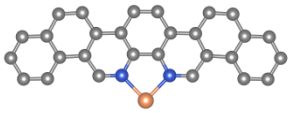 **Theoretical model 2**	−123.48	0.53	4.80
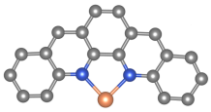 **Theoretical model 3**	−120.09	0.51	4.95

Table S12. The Structure Diagrams of Cu-N_1C_1 Structure with Ligands of Different Sizes (including [Cu-PhPy]$^+$, [Cu-Benzoquinoline]$^+$ and Theoretical Models), and the Charge on the Cu Center. Hydrogen Atoms were Omitted for Clarity.

Structure diagram	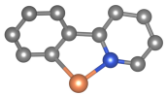 **[Cu-PhPy]$^+$**	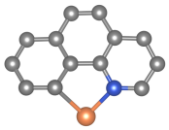 **[Cu-Benzoquinoline]$^+$**	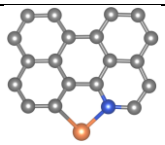 **Theoretical model 1**	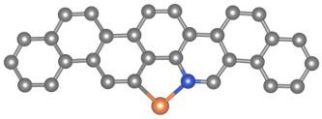 **Theoretical model 2**
Charge (|e|)	0.53	0.58	0.57	0.53

4. References

1. Gronert, S., Quadrupole ion trap studies of fundamental organic reactions. *Mass Spectrom. Rev.* 2005**, 24**, 100-120.
2. de Petris, G.; Cartoni, A.; Troiani, A.; Barone, V.; Cimino, P.; Angelini, G.; Ursini, O., Double C-H Activation of Ethane by Metal-Free SO_2^+ Radical Cations. *Chem. Eur. J.* 2010**, 16**, 6234-6242.
3. Parker, M. L.; Gronert, S., Investigating reduced metal species via sequential ion/ion and ion/molecule reactions: The reactions of transition metal phenanthrolines with allyl iodide. *Int. J. Mass spectrom.* 2017**, 418**, 73-78.
4. Borrome, M.; Gronert, S., Gas-Phase Dehydrogenation of Alkanes: C−H Activation by a Graphene-Supported Nickel Single-Atom Catalyst Model. *Angew. Chem. Int. Ed.* 2019**, 58**, 14906-14910.
5. Troiani, A.; Salvitti, C.; de Petris, G., Gas-Phase Reactivity of Carbonate Ions with Sulfur Dioxide: an Experimental Study of Clusters Reactions. *J. Am. Soc. Mass. Spectrom.* 2019**, 30**, 1964-1972.
6. Guo, M.; Wu, X.; Wu, H.; Sun, X., Ligand effect on Ru-centered species toward methane activation. *Phys. Chem. Chem. Phys.* 2024**, 26**, 14329-14335.
7. Waters, T.; O'Hair, R. A. J.; Wedd, A. G., Catalytic Gas Phase Oxidation of Methanol to Formaldehyde. *J. Am. Chem. Soc.* 2003**, 125**, 3384-3396.
8. Frisch, M. J.; Trucks, G. W.; Schlegel, H. B.; Scuseria, G. E.; Robb, M. A.; Cheeseman, J. R.; Scalmani, G.; Barone, V.; Petersson, G. A.; Nakatsuji, H.; Li, X.; Caricato, M.; Marenich, A. V.; Bloino, J.; Janesko, B. G.; Gomperts, R.; Mennucci, B.; Hratchian, H. P.; Ortiz, J. V.; Izmaylov, A. F.; Sonnenberg, J. L.; Williams; Ding, F.; Lipparini, F.; Egidi, F.; Goings, J.; Peng, B.; Petrone, A.; Henderson, T.; Ranasinghe, D.; Zakrzewski, V. G.; Gao, J.; Rega, N.; Zheng, G.; Liang, W.; Hada, M.; Ehara, M.; Toyota, K.; Fukuda, R.; Hasegawa, J.; Ishida, M.; Nakajima, T.; Honda, Y.; Kitao, O.; Nakai, H.; Vreven, T.; Throssell, K.; Montgomery Jr., J. A.; Peralta, J. E.; Ogliaro, F.; Bearpark, M. J.; Heyd, J. J.; Brothers, E. N.; Kudin, K. N.; Staroverov, V. N.; Keith, T. A.; Kobayashi, R.; Normand, J.; Raghavachari, K.; Rendell, A. P.; Burant, J. C.; Iyengar, S. S.; Tomasi, J.; Cossi, M.; Millam, J. M.; Klene, M.; Adamo, C.; Cammi, R.; Ochterski, J. W.; Martin, R. L.; Morokuma, K.; Farkas, O.; Foresman, J. B.; Fox, D. J. *Gaussian 16 Rev. A.03*, Wallingford, CT, 2016.
9. Adamo, C.; Barone, V., Toward reliable density functional methods without adjustable parameters: The PBE0 model. *J. Chem. Phys.* 1999**, 110**, 6158-6170.
10. Grimme, S.; Antony, J.; Ehrlich, S.; Krieg, H., A consistent and accurate ab initio parametrization of density functional dispersion correction (DFT-D) for the 94 elements H-Pu. *J. Chem. Phys.* 2010**, 132**.
11. Grimme, S.; Ehrlich, S.; Goerigk, L., Effect of the Damping Function in Dispersion Corrected Density Functional Theory. *J. Comput. Chem.* 2011**, 32**, 1456-1465.
12. Weigend, F.; Ahlrichs, R., Balanced basis sets of split valence, triple zeta valence and quadruple zeta valence quality for H to Rn: Design and assessment of accuracy. *Phys. Chem. Chem. Phys.* 2005**, 7**, 3297-3305.
13. Weigend, F., Accurate Coulomb-fitting basis sets for H to Rn. *Phys. Chem. Chem. Phys.* 2006**, 8**, 1057-1065.

14. Neese, F., Software update: the ORCA program system, version 4.0. *Wiley Interdiscip. Rev. Comput. Mol. Sci.* 2018**, 8**.
15. Dunning, T. H., Gaussian-basis sets for use in correlated molecular calculations .1. the atoms boron through neon and hydrogen. *J. Chem. Phys.* 1989**, 90**, 1007-1023.
16. Riplinger, C.; Sandhoefer, B.; Hansen, A.; Neese, F., Natural triple excitations in local coupled cluster calculations with pair natural orbitals. *J. Chem. Phys.* 2013**, 139**, 134101.
17. Guo, Y.; Riplinger, C.; Becker, U.; Liakos, D. G.; Minenkov, Y.; Cavallo, L.; Neese, F., Communication: An improved linear scaling perturbative triples correction for the domain based local pair-natural orbital based singles and doubles coupled cluster method DLPNO-CCSD(T). *J. Chem. Phys.* 2018**, 148**.
18. Lu, T.; Chen, F., Multiwfn: A multifunctional wavefunction analyzer. *J. Comput. Chem.* 2012**, 33**, 580-592.
19. Tirado-Rives J, Jorgensen W L. Performance of B3LYP density functional methods for a large set of organic molecules. *J. Chem. Theory Comput.* 2008, **4**, 297-306.
20. Munshi M U, Berden G, Oomens J. Infrared Ion Spectroscopy of Gaseous [Cu(2, 2′-Bipyridine)$_3$]$^{2+}$: Investigation of Jahn-Teller Elongation Versus Compression. *J. Phys. Chem. A,* 2025, **129,** 5, 1318-1327.
21. Bao, J. L. Zheng, J. Alecu, I. M. Lynch, B. J. Zhao, Y. Truhlar, D. G. Database of Frequency Scale Factors for Electronic Model Chemistries, Version 3 Beta 2. http://comp.chem.umn.edu/freqscale/ (accessed April 21, 2025).
22. Xiao M, Lu T. Generalized charge decomposition analysis (GCDA) method[J]. *J. Adv. Phys. Chem.* 2015, **4**, 111-124.
23. Momma, K.; Izumi, F., VESTA 3 for three-dimensional visualization of crystal, volumetric and morphology data. *J. Appl. Crystallogr.*2011**, 44**, 1272-1276.
24. Black, D. M.; Payne, A. H.; Glish, G. L., Determination of cooling rates in a quadrupole ion trap. *J. Am. Soc. Mass. Spectrom.* 2006**, 17**, 932-938.
25. Gronert, S., Estimation of effective ion temperatures in a quadrupole ion trap. *J. Am. Soc. Mass. Spectrom.* 1998**, 9**, 845-848.
26. Donald, W. A.; Khairallah, G. N.; O'Hair, R. A. J., The Effective Temperature of Ions Stored in a Linear Quadrupole Ion Trap Mass Spectrometer. *J. Am. Soc. Mass. Spectrom.* 2013**, 24**, 811-815.
27. Yang, Y. S.; Hsu, W. Y.; Lee, H. F.; Huang, Y. C.; Yeh, C. S.; Hu, C. H., Experimental and theoretical studies of metal cation-pyridine complexes containing Cu and Ag. *J. Phys. Chem. A* 1999**, 103**, 11287-11292.
28.DiMucci, I. M.; MacMillan, S. N.; Walroth, R. C.; Lancaster, K. M., Scrutinizing “Ligand Bands” via Polarized Single-Crystal X-ray Absorption Spectra of Copper(I) and Copper(II) Bis-2,2′-bipyridine Species. *Inorg. Chem.* 2020**, 59**, 13416-13426.
29. Grau, J.; Caubet, A.; Roubeau, O.; Montpeyó, D.; Lorenzo, J.; Gamez, P., Time-Dependent Cytotoxic Properties of Terpyridine-Based Copper Complexes. *ChemBioChem* 2020**, 21**, 2348-2355.
30. Guo, M.; Huang, B.; Yi, Q.; Luo, Z., Gas-phase synthesis and deposition of metal–bipyridine complex [M–bpy$_{1–2}$]$^+$ (M = Ag, Cu). *Phys. Chem. Chem. Phys.* 2021**, 23**, 16334-16340.
31. Zhou, M.; Andrews, L., Infrared spectra and density functional calculations of Cu(CO)$_{1–4}^+$, Cu(CO)$_{1–3}$, and Cu(CO)$_{1–3}^-$ in solid neon. *J. Chem. Phys.* 1999**, 111**, 4548-4557.

32. Lu, T.; Chen, Q., Simple, Efficient, and Universal Energy Decomposition Analysis Method Based on Dispersion-Corrected Density Functional Theory. *J. Phys. Chem. A* 2023**, 127**, 7023–7035.
33. Mitoraj, M. P.; Michalak, A.; Ziegler, T., A Combined Charge and Energy Decomposition Scheme for Bond Analysis. *J. Chem. Theory Comput.* 2009**, 5**, 962-975.
34. Tian, L. U.; Fei-Wu C., Comparison of Computational Methods for Atomic Charges. *Acta Phys.-Chim. Sin.* 2012**, 28**, 1-18.
35. Qingyu L.; Shenggui H., Oxidation of Carbon Monoxide on Atomic Clusters. Chemical Journal of Chinese Universities, 2014, **35**, 665-688.
36. Nesbitt D J, Field R W. Vibrational energy flow in highly excited molecules: role of intramolecular vibrational redistribution. *J. Phys. Chem.*, 1996, **100**, 12735-12756.
37. Eckhard J F, Neuwirth D, Panosetti C, et al. Consecutive reactions of small, free tantalum clusters with dioxygen controlled by relaxation dynamics. *Phys. Chem. Chem. Phys.*, 2017, **19**, 5985-5993.
38. Eckhard J F, Neuwirth D, Tschurl M, et al. From oxidative degradation to direct oxidation: size regimes in the consecutive reaction of cationic tantalum clusters with dioxygen. *Phys. Chem. Chem. Phys.* 2017, **19**, 10863-10869.
39. Zhou M, Andrews L, Bauschlicher C W. Spectroscopic and theoretical investigations of vibrational frequencies in binary unsaturated transition-metal carbonyl cations, neutrals, and anions. *Chem. Rev.,* 2001, **101**, 1931-1962.
40. Goldman A S, Krogh-Jespersen K. Why do cationic carbon monoxide complexes have high C−O stretching force constants and short C-O bonds? Electrostatic effects, not σ-bonding[J]. J.Am.Chem.Soc., 1996, **118**, 12159-12166.
41. Lupinetti, A. J.; Fau, S.; Frenking, G.; Strauss, S. H. Theoretical analysis of the bonding between CO and positively charged atoms. *J. Phys. Chem. A*, 1997, **101**, 9551−9559.
42. Chen D, Zhang L H, Du J, et al. A tandem strategy for enhancing electrochemical CO2 reduction activity of single-atom Cu-S_1N_3 catalysts via integration with Cu nanoclusters. *Angew. Chem.* 2021, **133**, 24224-24229.
43. Yang T, Mao X, Zhang Y, et al. Coordination tailoring of Cu single sites on C3N4 realizes selective CO2 hydrogenation at low temperature. *Nat. Commun.* 2021, **12**, 6022.
44. Shi H, Wang H, Zhou Y, et al. Atomically dispersed indium-copper dual-metal active sites promoting C− C coupling for CO2 photoreduction to ethanol. Angewandte Chemie, 2022, **134**, e202208904.
45. Wu H, Tian B, Xu W, et al. Pressure-Dependent CO_2 Electroreduction to Methane over Asymmetric Cu–N_2 Single-Atom Sites. *J. Am. Chem. Soc.* 2024, **146**, 22266-22275.
46. Nielsen N D, Smitshuysen T E L, Damsgaard C D, et al. Characterization of oxide-supported Cu by infrared measurements on adsorbed CO. *Surf. Sci.* 2021, **703**, 121725.